

# Optical Nonlinearity Enabled Super-Resolved Multiplexing Microscopy

Lei Ding, Chaohao Chen,\* Xuchen Shan, Baolei Liu, Dajing Wang, Ziqing Du, Guanshu Zhao, Qian Peter Su, Yang Yang, Benjamin Halkon, Toan Trong Tran, Jiayan Liao, Igor Aharonovich, Min Zhang, Faliang Cheng,\* Lan Fu,\* Xiaoxue Xu,\* and Fan Wang\*

Optical multiplexing for nanoscale object recognition is of great significance within the intricate domains of biology, medicine, anti-counterfeiting, and microscopic imaging. Traditionally, the multiplexing dimensions of nanoscopy are limited to emission intensity, color, lifetime, and polarization. Here, a novel dimension, optical nonlinearity, is proposed for super-resolved multiplexing microscopy. This optical nonlinearity is attributable to the energy transitions between multiple energy levels of the doped lanthanide ions in upconversion nanoparticles (UCNPs), resulting in unique optical fingerprints for UCNPs with different compositions. A vortex beam is applied to transport the optical nonlinearity onto the imaging point-spread function (PSF), creating a robust super-resolved multiplexing imaging strategy for differentiating UCNPs with distinctive optical nonlinearities. The composition information of the nanoparticles can be retrieved with variations of the corresponding PSF in the obtained image. Four channels multiplexing super-resolved imaging with a single scanning, applying emission color and nonlinearity of two orthogonal imaging dimensions with a spatial resolution higher than 150 nm ( $1/6.5\lambda$ ), are demonstrated. This work provides a new and orthogonal dimension – optical nonlinearity – to existing multiplexing dimensions, which shows great potential in bioimaging, anti-counterfeiting, microarray assays, deep tissue multiplexing detection, and high-density data storage.

and biological systems.<sup>[5,6]</sup> It provides the ability to encode multiple information into a single image, allowing for high information density and simultaneous identification of multiple targeted chemicals and biomolecules.<sup>[6,9,10]</sup> To achieve this, encoding dimensions such as emission intensities,<sup>[5,11]</sup> colors,<sup>[12,13]</sup> lifetimes,<sup>[2,7]</sup> and polarizations<sup>[3,4,14]</sup> have been explored individually or in combination, enhancing the capabilities of multiplexed imaging.


The development of super-resolution microscopy has revolutionized imaging at the nanoscale by surpassing the diffraction limit of conventional light microscopy.<sup>[15–19]</sup> This breakthrough opens up opportunities for multiplexed imaging to enable simultaneous differentiation and imaging of multiple targets at the nanoscale. Multicolor single-molecule localization microscopy<sup>[17,20]</sup> and stimulated emission depletion microscopy<sup>[21,22]</sup> have facilitated the visualization of molecular assemblies within cells by utilizing distinct fluorescent probes with different emission spectra. Due to its robust lifetime-based target identification, DNA point accumulation for imaging

in nanoscale topography<sup>[10,22,23]</sup> excels in dense and sticky cellular environments. Utilizing orbital-angular-momentum-dependent polarization and combined with wavelength and three

## 1. Introduction

Multiplexed optical imaging<sup>[1–8]</sup> has emerged as a powerful technique with applications in data storage,<sup>[1–3]</sup> anti-counterfeiting,<sup>[4]</sup>

L. Ding, C. Chen, M. Zhang, F. Cheng  
Guangdong Engineering and Technology Research Center for Advanced Nanomaterials  
School of Environment and Civil Engineering  
Dongguan University of Technology  
Dongguan 523808, China  
E-mail: chaohao.chen@anu.edu.au; chengfl@dgut.edu.cn

 The ORCID identification number(s) for the author(s) of this article can be found under <https://doi.org/10.1002/adma.202308844>

© 2023 The Authors. Advanced Materials published by Wiley-VCH GmbH. This is an open access article under the terms of the Creative Commons Attribution License, which permits use, distribution and reproduction in any medium, provided the original work is properly cited.

DOI: 10.1002/adma.202308844

L. Ding, Q. P. Su, X. Xu  
School of Biomedical Engineering  
Faculty of Engineering and IT  
University of Technology Sydney  
NSW 2007, Australia  
E-mail: xiaoxuehelen.xu@uts.edu.au

C. Chen, L. Fu  
Australian Research Council Centre of Excellence for Transformative Meta-Optical Systems  
Department of Electronic Materials Engineering  
Research School of Physics  
The Australian National University  
Canberra, ACT 2600, Australia  
E-mail: lan.fu@anu.edu.au

spatial dimensions shows the viability of nanoscale information multiplexing and even 6D optical information multiplexing.<sup>[4]</sup> Despite these accomplishments, increasing the number of encoded channels within a single dimension remains a challenge in super-resolved multiplexing imaging. Developing novel encoding dimensions could be multiplied to enhance the information encoding capabilities and is critical for the further development of super-resolved multiplexed imaging.

Lanthanide-doped upconversion nanoparticles (UCNPs)<sup>[7,24–27]</sup> have garnered significant attention for multiplexed imaging at the nanoscale, owing to their strong anti-Stokes emission and unique nonlinear optical response.<sup>[16,28,29]</sup> The optical nonlinearity of UCNPs has been exploited to achieve super-resolution imaging.<sup>[28,30–32]</sup> However, the powerful optical nonlinearity of UCNPs has yet to be fully harnessed as a dimension for multiplexing purposes, primarily due to the extensive time required to obtain the comprehensive power-dependent curve.<sup>[32,33]</sup>

In this work, we present a new dimension for super-resolved multiplexing microscopy by exploiting the nonlinear optical response under a vortex beam excitation. The optical nonlinearity in UCNPs exhibits distinct “fingerprints” based on different compositions, sizes, surface modifications, or dopant concentrations. By analyzing variations in the effective point-spread functions (PSFs), we demonstrate that the vortex-beam-based point-scanning approach offers an effective and efficient way to extract optical nonlinearity from samples. Incorporating nonlinear optical response and vortex beams simplifies the optical setup, enables compatibility with existing microscopy systems, and facilitates the extraction of nonlinear response information. By employing the nonlinearity feature in multiplexing imaging, our work opens up exciting new possibilities for future development of super-resolved microscopy for nanoscale object recognition.

## 2. Result

The UCNPs are composed of a crystal host structure and thousands of guest lanthanide ions that provide a high degree of flexibility in engineering their optical properties due to the special

light–matter interaction.<sup>[24,25]</sup> The lanthanide ions possess multiple intermediate energy states with long lifetimes, facilitating energy transfers and resulting in upconversion emissions from near-infrared to visible and ultraviolet regions (**Figure 1a**). In the case of Yb<sup>3+</sup>/Tm<sup>3+</sup> dual-doped UCNPs, Yb<sup>3+</sup> partially replaces Y<sup>3+</sup> ions within the crystal lattice of the host material. The Yb<sup>3+</sup> ions, acting as sensitizers, absorb incident photons and transfer the energy to the adjacent Tm<sup>3+</sup> ions. The Tm<sup>3+</sup> ion has multiple intermediate energy levels, enabling efficient energy transfer processes and various relaxation mechanisms within the system, ultimately leading to upconverted emission. Due to the intricate nature of energy transitions in UCNP, the emitted fluorescence intensity exhibits a nonlinear power-dependent response (**Figure 1c**),<sup>[15,16,28–33]</sup> where the increase in excitation power does not correspond linearly to the increase in emission intensity. At high excitation powers, the emission intensity cannot increase further, and the saturation effect occurs due to the limited population of emitter ions. This optical nonlinearity arises from the energy transitions that occur between the multiple energy levels of the doped lanthanide ions in UCNPs. Consequently, UCNPs, synthesized with different compositions, sizes, surface modifications, or dopant concentrations, can exhibit distinct “fingerprints” in terms of their optical nonlinearities.<sup>[15]</sup> In addition to the four conventional optical dimensions (**Figure 1b**), optical nonlinearity enables a new dimension of optical multiplexing, bringing possibilities for nanoscale sample discernment and classification.

The typical method to acquire the optical nonlinearity for UCNPs involves measuring the fluorescence intensity as a function of the excitation power (**Figure 1c**). Numerous measurements or average data points are required to account for the fluctuations in the fluorescence signal, which is a time-consuming operation. Our previous work has shown that the optical nonlinearity behavior in UCNPs can have implications for the effective PSF in point-scanning-based fluorescence microscopy.<sup>[28]</sup> Optical nonlinearity leads to changes in the profile of the PSF. The effective PSF ( $h_{\text{eff}}(x, y)$ ) can be described as<sup>[34]</sup>

$$\begin{cases} h_{\text{eff}}(x, y) = h_{\text{em}}(x, y) \times [h_{\text{dec}}(x, y) * p_h(d)] \\ h_{\text{em}}(x, y) = \eta(i) \times h_{\text{exc}}(x, y) \end{cases} \quad (1)$$

where  $h_{\text{em}}(x, y)$  is the PSF of emission,  $h_{\text{dec}}(x, y)$  is the PSF of the detection system,  $h_{\text{exc}}(x, y)$  is the PSF of the excitation beam, and  $\eta(i)$  is the excitation-power-dependent emission intensity curve, and  $p_h(d)$  is the spatial transmission function of the pinhole.

Although the PSF appears as a Gaussian shape in a conventional confocal configuration (**Figure 1d**), optical nonlinearity effects may affect the fluorescence intensity and spatial localization<sup>[28]</sup> (**Figures S8–S12, Supporting Information**). These nonlinearity-induced variations from different types of UCNPs can be quantified by analyzing parameters such as cross-section profiles and full width at half-maximum (FWHM). However, these variations are too subtle to be extracted and easily overwhelmed by background noise during the experimental acquisition, including shot noise, autofluorescence, and detector read-out noise. This is because the relevant nonlinear information is primarily preserved in the outer PSF when under Gaussian beam excitation, which can be easily compromised by the detection PSF (**Figure S6, Supporting Information**). By contrast, when

C. Chen, G. Zhao, Y. Yang, T. T. Tran  
School of Electrical and Data Engineering  
Faculty of Engineering and Information Technology  
University of Technology Sydney  
NSW 2007, Australia

X. Shan, B. Liu, D. Wang, F. Wang  
School of Physics  
Beihang University  
Beijing 100191, China  
E-mail: fanwang@buaa.edu.cn

Z. Du, J. Liao, I. Aharonovich  
School of Mathematical and Physical Sciences  
Faculty of Science  
University of Technology Sydney  
NSW 2007, Australia

B. Halkon  
Centre for Audio  
Acoustics and Vibration  
Faculty of Engineering and IT  
University of Technology Sydney  
Ultimo, NSW 2007, Australia

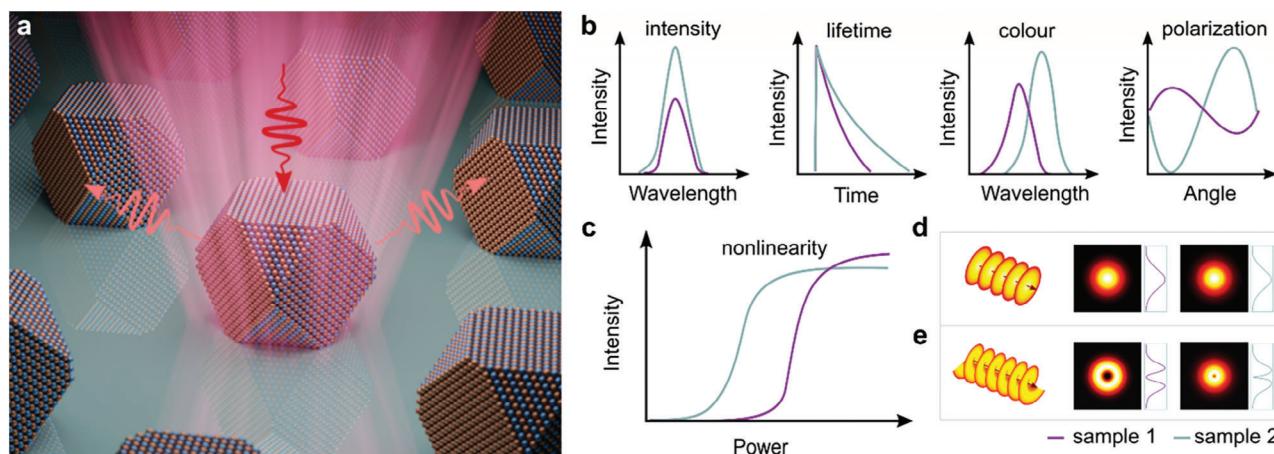


**Figure 1.** Optical nonlinearity for multiplexed imaging. a) Illustration of nonlinear emission of lanthanide-doped nanoparticles under near-infrared excitation. b) Four traditional optical dimensions for encryption and decryption. c) Optical nonlinearity as a dimension for multiplexed imaging. d,e) The point-spread functions (PSF) of emission from two types of nanoparticles excited by a Gaussian beam and vortex beam, respectively. The corresponding cross-section profiles are shown on the right.

utilizing a vortex beam for excitation, the information is retained not only in the outer region but also prominently in the middle of the PSF. This distinction allows the vortex beam to capture and preserve nonlinear information more effectively. Therefore, we introduce a vortex beam to overcome the challenge of extracting and quantifying the optical nonlinearity (Figure 1e). The vortex beam is created by applying a vortex phase plate to generate a helical wavefront, resulting in a doughnut-shaped intensity distribution at the focus point. This doughnut-shaped beam has a dark spot in the center, which corresponds to a lower energy level than the surrounding region. When interacting with nanoparticles, the unique intensity distribution in the doughnut beam can lead to more significant changes in PSF compared to the Gaussian beam (Figure 1e).

### 2.1. PSF Engineering of UCNPs under Vortex Beam

We first investigate the variations in the PSF under a vortex beam to gain insights into the underlying mechanism of optical-nonlinearity-based multiplexing. We modify the traditional confocal microscope configuration with a vortex phase plate that induces a phase shift, transforming the Gaussian beam into a doughnut-shaped intensity distribution (Figure 2a and Figure S2 (Supporting Information)). For  $\text{Yb}^{3+}/\text{Tm}^{3+}$ -UCNPs ( $\text{NaYF}_4:20\text{Yb}^{3+}/4\text{Tm}^{3+}$ , with a diameter of 45 nm, Figure S1, Supporting Information), the presence of multiple long-lived intermediate states allows for the efficient transfer of sensitized photons to the energy levels of  $\text{Tm}^{3+}$  emitters. This sequential energy transfer process ultimately enables the emission of upconverted photons through two-photon excitation (Figure 2b,  $^3\text{H}_4 \rightarrow ^3\text{H}_6$ ) and three or four-photon excitations (Figure 2b,  $1\text{D}_2 \rightarrow ^3\text{F}_4$  and  $^1\text{G}_4 \rightarrow ^3\text{H}_6$ ). The multistep of photon absorption and transfer leads to the unique optical response showcasing a nonlinear power-dependent curve at 800 nm (Figure 2c). Although fluctuations in the measured intensities could be attributed to the precise alignment of the system's focus, postnormalization analysis reveals a remarkable uniformity in their nonlinearity, further

affirming the potential to utilize nonlinearity as a dimension for multiplexing.

Considering the signal-to-noise ratio, we choose the excitation power range from 7 to 2 mW. Compared to the excitation with a Gaussian beam (Figure 2d, top; Figures S8–S12 (Supporting Information)), the PSF of a single nanoparticle generated by the doughnut-shaped beam exhibits distinct variations along the excitation intensities (Figure 2d, bottom; Figures S13–S15 (Supporting Information)). In the higher excitation power regime where the emission saturation effect occurs, the doughnut-shaped PSF's dark spot becomes smaller and resembles the one produced under a Gaussian beam.<sup>[29]</sup> As the excitation power decreases, the distinctive doughnut-shaped feature of the PSF becomes more apparent. This excitation-intensity-related change in PSF clearly indicates the influence of optical nonlinearity. The variations in the PSF are further verified by examining the cross-profiles of the PSF (Figure 2d), where the middle valley becomes larger and deeper as the excitation power is reduced.

The emission PSF under the vortex beam at a certain excitation power density is essentially determined by the nonlinear response curve (Figure 3). There are three distinctive features from the curve that significantly affect the appearance of PSF. First, we have the power point ( $I_S$ ), which represents the threshold to achieve half value of the maximum emission intensity. Second, the power point ( $I_{MAX}$ ) is crucial in determining the maximum emission intensity with fixed  $I_S$ . In other words, a smaller  $I_{MAX}$  indicates a more superlinear shape of the curvature between  $I_S$  and  $I_{MAX}$ . Finally, the onset value of the curve, defined as the power point (in unit of  $I_S$ ) required to achieve  $e^{-2}$  of the maximum emission intensity, is another key factor. A larger onset indicates more sublinear shape of the curvature between 0 and  $I_S$ . Lower values of  $I_S$  and/or  $I_{MAX}$  result in a reduction in size of dark spot, which we measure full width at half-maximum of the dip at the doughnut PSF. Conversely, a larger onset of the nonlinearity curve results in a greater height of the dip compared to the counterparts.

We further quantitatively characterize the optical nonlinearity of the UCNPs by analyzing the features in the PSF. We

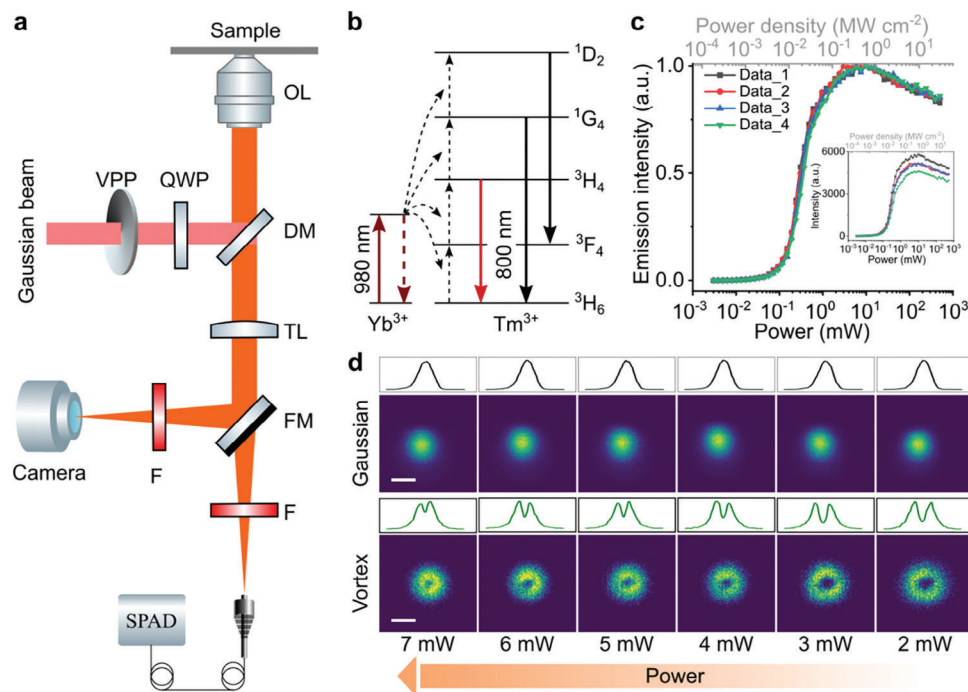


**Figure 2.** Optical-nonlinearity-induced PSF fluctuation under vortex beam. a) Optical configuration of the single-vortex-beam confocal microscope. OL, objective lens; DM, dichroic mirror; F, filter; TL, tube lens; SPAD, single-photon avalanche detector; VPP, vortex-phase plate; QWP, quarter-wave plate. b) The simplified energy levels and upconversion process of Yb<sup>3+</sup> and Tm<sup>3+</sup> dual-doped UCNPs. c) The normalized power-dependent emission intensity curves at 800 nm. Inset, the four original nonlinearity curves. d) PSF and the corresponding cross-section profile variations of a single UCNPs with Gaussian beam (top) and vortex beam (bottom) under different laser intensities (see Note S3 in the Supporting Information). Scale bars are 500 nm.

utilize three types of UCNPs (NaYF<sub>4</sub>:20Yb<sup>3+</sup>/2Tm<sup>3+</sup>, 50 nm; NaYF<sub>4</sub>:20Yb<sup>3+</sup>/4Tm<sup>3+</sup>, 45 nm; and NaYF<sub>4</sub>:40Yb<sup>3+</sup>/4Tm<sup>3+</sup>, 25 nm, see Figure S1 in the Supporting Information). All the nanoparticles utilized in our work exhibit a  $\beta$ -phase spherical-like morphology. Given this uniform morphology, the influence of morphology can be considered negligible. The variation in doping concentration and particle size in our research is primarily designed to achieve similar emission intensities while maintaining distinct nonlinearities. Figure 3a provides a schematic representation of the crystal structure, showing the partial replacement of Y<sup>3+</sup> ions with Yb<sup>3+</sup> and/or Tm<sup>3+</sup> ions. As reported in our previous work,<sup>[15,18]</sup> the variability of the optical nonlinear response curves (800 nm emission band) among different UCNPs can be tuned by adjusting the doping concentration of sensitizers and emitters or by introducing a core-shell structure (Figure 3b). UCNPs with a lower Tm<sup>3+</sup> doping concentration exhibit characteristics that lead to their easier saturation with lower values of  $I_S$  and  $I_{MAX}$  due to the reduced energy transfer ratio and subsequent decline in the saturated carrier flow rate, which is proportional to the laser-induced carrier generation rate. By contrast, higher concentrations of Tm<sup>3+</sup> reduce the average distance between the sensitizer and activator ions within the crystal structure. This proximity enhances the energy transfer ratio's efficiency and increases the cross-relaxation rate.<sup>[35,36]</sup> Consequently, higher-doping UCNPs demonstrate a sharper curvature at the onset of their nonlinearity curves, but with higher  $I_S$  and  $I_{MAX}$  values.

By optimizing the vortex beam excitation intensity to 2 mW, we achieve distinct features in the PSFs of the three categories of UCNPs (Figure 3c and Figures S13–S15 and Tables S2–S4

(Supporting Information)). For the low-concentration (2%) Tm-doped nanoparticles, the earlier saturation behavior results in nearly Gaussian-shaped cross-section profiles due to oversaturation (Figure 3c, left), whereas the 40Yb<sup>3+</sup>/4Tm<sup>3+</sup> nanoparticles exhibit a doughnut-shaped PSF, characterized by a cross-section profile with a middle-valley shape (Figure 3c, middle). Due to the limited number of absorbed photons, the 20Yb<sup>3+</sup>/4Tm<sup>3+</sup> samples undergo more pronounced features, with a larger doughnut hole in the PSF and a collapsed cross-section profile (Figure 3c, right). The experimental measurements are consistent with our numerical simulation results (Figure 3d), providing further validation for nonlinearity-based multiplexing imaging approach. Notably, the slight discrepancy in PSF shapes between the experimental and simulation results is mainly due to the noise and system alignment disparities. To quantitatively distinguish between different PSFs, we focus on three key parameters: 1) the outside FWHM (Figure 3e); 2) the internal FWHM (iFWHM, Figure 3f); 3) the height of the middle dip (Height, Figure 3g). We employ a cross-validation method with a convolutional neural network (CNN) that integrates all three characterizations, achieving more precise recognition of specific nanoparticle types automatically (Figures S16 and S17, Supporting Information).

## 2.2. Multiplexing of Dopant Types under Vortex Beam

Next, we conduct simulations and experiments to distinguish two categories of UCNPs to validate the effectiveness of the optical-nonlinearity-based multiplexing techniques. To facilitate the

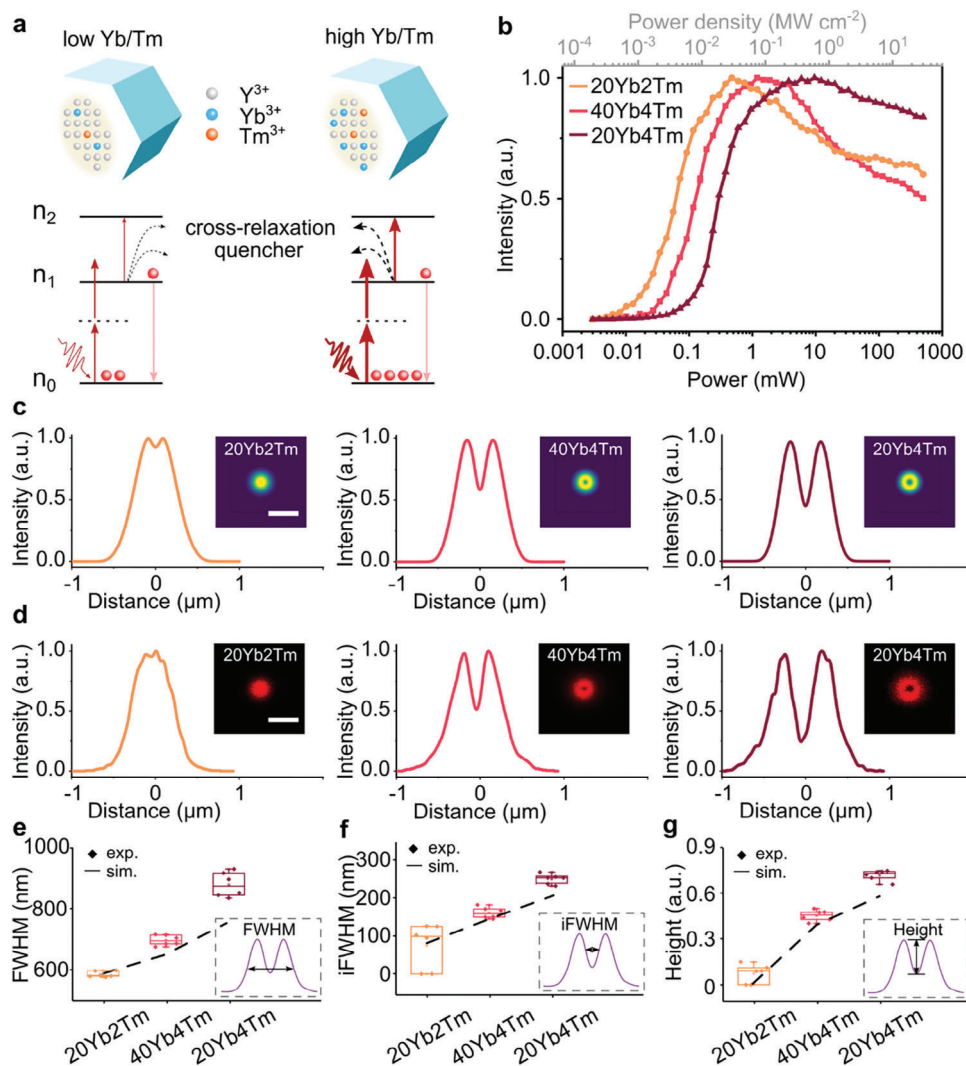


**Figure 3.** Quantitative analysis of the PSFs for determination. a) Schematic of different doping concentrations (top) and the corresponding energy transfer (bottom). For similar emission intensity, low doping nanoparticle requires low photon absorption and experiences less quenching and cross-relaxation, vice versa. b) The nonlinear power-dependent emission curves of three single UCNPs ( $\text{NaYF}_4\text{:}20\text{Yb}/2\text{Tm}$ , 50 nm,  $\text{NaYF}_4\text{:}20\text{Yb}/4\text{Tm}$ , 45 nm,  $\text{NaYF}_4\text{:}40\text{Yb}/4\text{Tm}$ , 25 nm, size is in diameter) measured at the 800 nm (BPF2, ET805/20M, Chroma) peak. c,d) The simulation (c) and experimental (d) cross-section line profiles of the PSF of UCNPs (shown as insets) under a 980 nm vortex beam excitation with a power at 2 mW (power density, see Note S3 in the Supporting Information). e–g) The three characteristic parameters for quantitative analysis, including full width at half-maximum (FWHM), internal FWHM (iFWHM), and height of the middle dip, respectively. The parameters were measured from the experimental and simulation PSFs. Boxplots are based on 6 samples. Scale bars are 1  $\mu\text{m}$ .

verification of the nonlinearity multiplexing results, we intentionally utilize two different emitter ions,  $\text{Tm}^{3+}$  and  $\text{Er}^{3+}$ , which both produce distinct wavelengths of emissions. This approach allows us to directly confirm our findings through separate color channels, providing a rigorous and robust verification procedure. The advanced synthesis method ensures the uniformity in both morphology and size of single UCNPs, enabling to obtain the desired similar emission intensities for Tm- and Er-doped UCNPs:  $\text{NaYF}_4\text{:}48\text{Yb}^{3+}/4\text{Tm}^{3+}$  (denoted as Tm-UCNP) with a diameter of 37 nm and  $\text{NaYF}_4\text{:}48\text{Yb}^{3+}/2\text{Er}^{3+}$  (denoted as Er-UCNP) with a diameter of 38 nm (Figure S1, Supporting Information). Under 980 nm laser excitation, Tm-UCNP and Er-UCNP show different optical nonlinearity behaviors due to discrepancies in their energy transfer and emission efficiency. Tm-UCNP has a

lower threshold and saturates earlier with a steeper slope compared to its competitor in the power-dependent curves (Figure 4a). This difference in optical nonlinearity will cause variations in the PSF when modulating from Gaussian to vortex beam excitation. We first acquire the confocal images of the mixed samples with an 842 short pass filter by scanning a standard Gaussian excitation beam (Figure 4b,c, left). Neither the simulation result nor the experimental image provides enough heterogeneous features to differentiate between the two types of UCNPs due to the inconspicuous distinction of signals drowned in the noise. By contrast, the PSF becomes distinguishable when excited by a vortex beam. Tm-UCNPs exhibit PSF with a small doughnut hole, while Er-UCNPs exhibit a larger one, allowing for the recognition of nanoparticles presented as magenta and mint, respectively. This

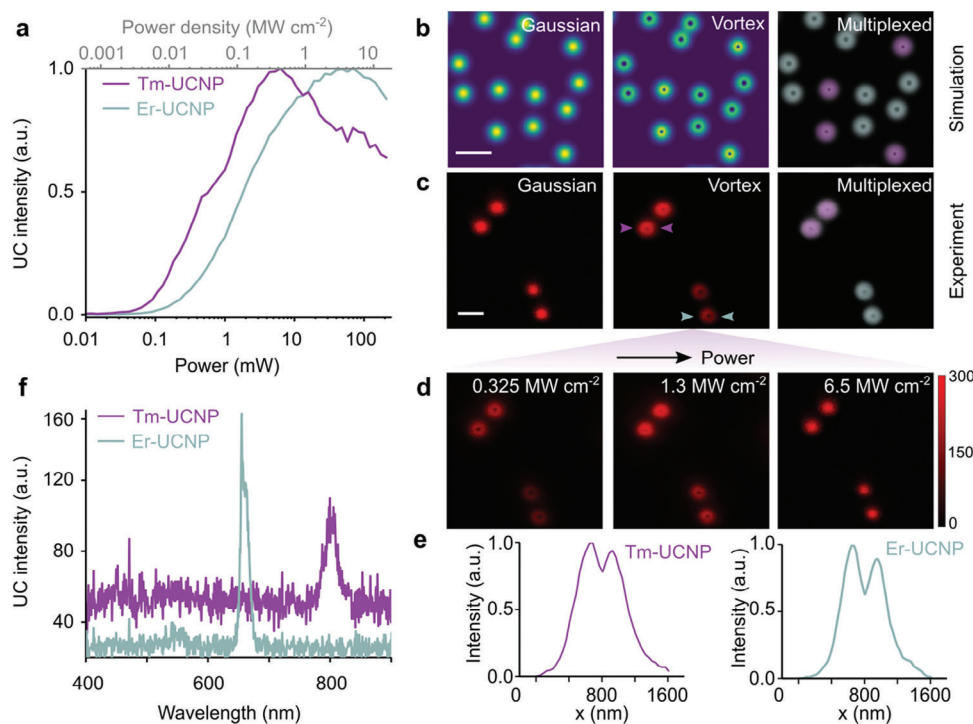


**Figure 4.** Super-resolved multiplexing of UCNP with different dopant types. a) Nonlinear power-dependent curves of Tm-UCNP and Er-UCNP. b,c) Multiplexed image of the mixture of Tm-UCNPs and Er-UCNPs by simulation (b) and experiment (c). Images are obtained under the Gaussian beam (left), and vortex beam (middle), respectively. The decoded results (right) are labeled with false colors for recognized particle types, where magenta represents Tm-UCNP and mint represents Er-UCNP. Laser power density is  $0.65 \text{ MW cm}^{-2}$ . d) PSF variations of UCNP in (c) under vortex beam with increasing power densities. e) The intensity profiles in (c). Left is Tm-UCNP and right is Er-UCNP. f) The corresponding spectrum of single Tm-UCNP and Er-UCNP in (c) with laser power density at  $0.13 \text{ MW cm}^{-2}$ . Scale bars are  $1 \mu\text{m}$ .

makes our strategy advantageous to the intensity-based methods where feeble intensity difference is usually buried in the noise or signal fluctuation, while the feature of nonlinearity still remains outstanding.

We optimize excitation power density for enhanced visibility of PSF differences, as shown in Figure 4d. Increasing the excitation power enhances the emission intensity for both Tm- and Er-UCNPs, but this intensity change does not impact the differentiation of Tm- and Er-UCNPs when considering the normalized PSF. However, at high excitation power levels, such as  $6.5 \text{ MW cm}^{-2}$ , the image PSFs transition from doughnut-shaped to Gaussian (as shown in Figure 4d) due to the saturation characteristics exhibited by both nanoparticle types. This Gaussian PSF makes it impossible to use iFWHM and Height (as demonstrated in Figure 3e) for nanoparticle differentiation. Therefore, it is essential to maintain excitation power below the point of oversaturation to preserve the ability to compare the carried nonlinearity information within the PSF's central region. It is worth noting that the excitation power was chosen to ensure a favorable signal-to-noise ratio for imaging. For distinguishing the two types of UCNP,  $0.65 \text{ MW cm}^{-2}$  (Figure 4c, middle) represents the optimized excitation power. Therefore, the variable degrees of saturating emission PSFs are crucial for optical-nonlinearity-based multiplexing. It is essential to carefully choose the excitation power and optimize imaging parameters to mitigate the effects of oversaturation for optical-nonlinearity-based multiplexing.

Furthermore, we show the capacity to quantify nanoparticle recognition by analyzing the intensity profiles throughout the PSF (Figure 4e and Table S5 (Supporting Information)). Due to the different energy level distributions in  $\text{Tm}^{3+}$  and  $\text{Er}^{3+}$ , Tm-UCNP emits at a wavelength of  $800 \text{ nm}$ , whereas Er-UCNP at a wavelength of  $650 \text{ nm}$  (Figure S18, Supporting Information). Therefore, we can employ single-particle spectroscopy to validate the recognition results, as shown in Figure 4f. Additionally, confocal images using  $800$  and  $650 \text{ nm}$  band pass filters coincide with the discernment obtained by the nonlinearity-based strategy (Figure S19, Supporting Information). Compared to the Gaussian beam, the vortex beam contains more information at high spatial frequencies,<sup>[29]</sup> allowing for super-resolved multiplexing imaging beyond the diffraction limit.

### 2.3. Particle Classification

To demonstrate the capability of our proposed method for super-resolved multiplexing, our innovative approach facilitates the simultaneous acquisition of signals across two orthogonal dimensions (emission color and nonlinearity), with a total of 4 channels of multiplexed super-resolved imaging. We perform point-scanning imaging with a mixture of four types of nanoparticles. The monochrome Gaussian-beam image obtained from this mixture shows multiple nanoparticles but lacks discernible features to distinguish the particle information (Figure 5a), while

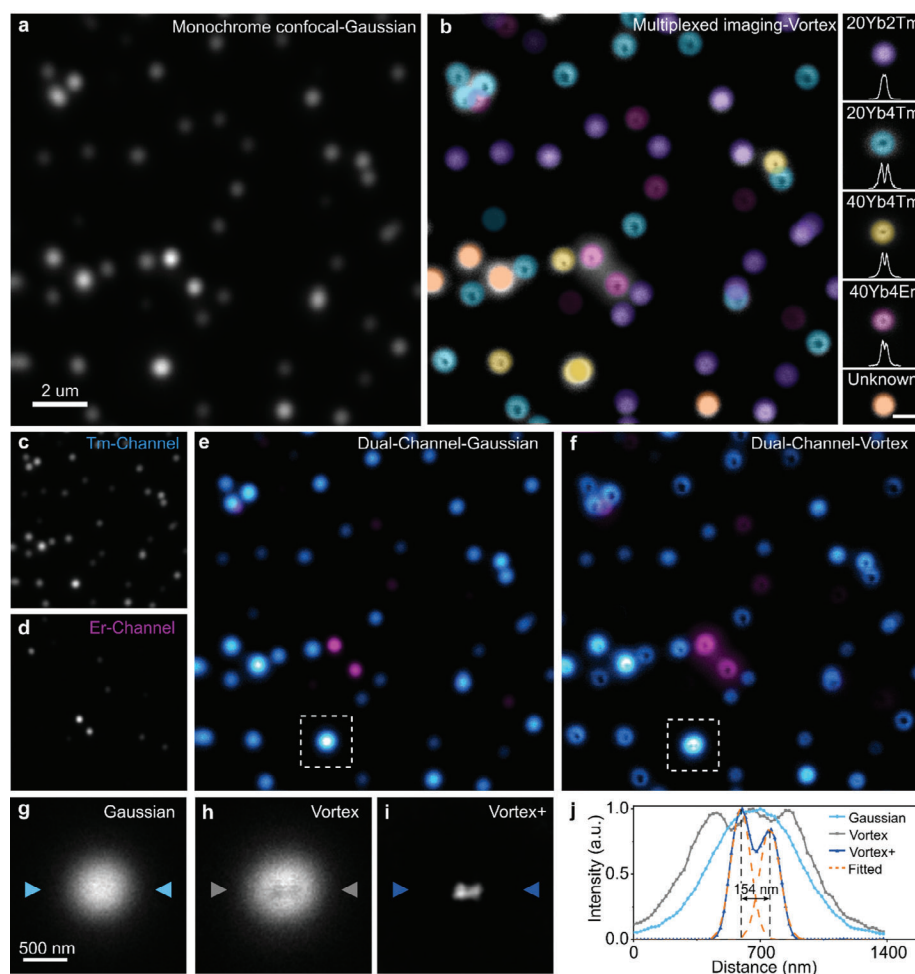


**Figure 5.** Super-resolved multiplexing of mixed UCNPs. a) The monochrome confocal imaging of the mixture of four types of UCNPs under Gaussian-beam excitation at 2 mW (power density, see Note S3 in the Supporting Information). The emission was obtained with an 842 nm short-pass filter. UCNPs ( $\text{NaYF}_4\text{:}20\text{Yb}/2\text{Tm}$ , 50 nm;  $\text{NaYF}_4\text{:}20\text{Yb}/4\text{Tm}$ , 45 nm;  $\text{NaYF}_4\text{:}40\text{Yb}/4\text{Tm}$ , 25 nm;  $\text{NaYF}_4\text{:}40\text{Yb}/4\text{Er}$ , 50 nm, size is in diameter). b) The corresponding super-resolved multiplexed imaging under the vortex-beam excitation. On the right are the matching color markers, and the cross-section profiles. The orange indicates the unresolved samples. c,d) The confocal imaging in Tm-Channel (800 nm emission) and Er-Channel (650 nm emission) of the mixture under 980 nm Gaussian-beam excitation, respectively. e) The Dual-Channel image by merging Tm-Channel in (c) and Er-Channel in (d). f) The corresponding Dual-Channel image under the vortexed-beam excitation. g–i) The magnified area of interest to illustrate the super-resolution imaging capability. j) Line profiles in (g–i). Pixel dwell time: 1 ms. Pixel size: 20 nm. Scale bars: 1  $\mu\text{m}$  in (b).

the multiplexed image collected with the vortex beam provides significant distinguishing characteristics with different PSFs (Figure 5b). Based on the nonlinear characteristics of particle species, we can conveniently classify the particle doping information (Figure 5b). We label the particles with purple, green, blue, and red for  $\text{NaYF}_4\text{:}20\text{Yb}^{3+}/2\text{Tm}^{3+}$ ,  $\text{NaYF}_4\text{:}20\text{Yb}^{3+}/4\text{Tm}^{3+}$ ,  $\text{NaYF}_4\text{:}40\text{Yb}^{3+}/4\text{Tm}^{3+}$ , and  $\text{NaYF}_4\text{:}40\text{Yb}^{3+}/4\text{Er}^{3+}$ , respectively. Due to the resolution limitation, the unresolved samples are marked with orange. For multiplexed imaging, signal capturing with multiple imaging channels orthogonally in different dimensions is imperative. The color dimension encompasses two distinct channels operating at the wavelength of 800 nm (Figure 5c) and 650 nm (Figure 5d), respectively, which allows simultaneous dual-channel fluorescence imaging (Figure 5e). By combining color-based signal acquisition at specific wavelengths (800 and 650 nm) with the exploitation of nonlinearity effects in the optical response, we achieve an enhancement in mul-

tiplexed imaging capabilities (Figure 5f). Within the 800 nm channel, we introduce three separate nonlinearity channels, each revealing different responses based on incident light intensity. Furthermore, we resolve two adjacent nanoparticles within the diffraction limit (Figure 5g–i), demonstrating the feasibility of this optical-nonlinearity-based multiplexed imaging with spatial super-resolution of 154 nm (Figure 5j). The cross-section profiles demonstrate an approximately threefold enhancement in resolution.

### 3. Conclusion

In conclusion, this work presents a novel strategy for super-resolved optical multiplexing imaging by utilizing the optical nonlinearity behavior of UCNPs with vortex beam excitation. By manipulating the doping concentrations and dopant types in UCNPs, we can control the nonlinear response characteristics.

Unlike previous multiplexing techniques that rely on specific points of the response curves,<sup>[11,37]</sup> our method uses the full power-dependent fluorescent curves to accurately recognize the discern nanoparticles at the nanoscale. The use of a single-vortex-beam scanning mode with a simplified optics setup makes this method compatible with standard commercial or lab-based laser scanning microscopes, addressing the complexity and stability issues associated with existing systems. The inherent potential of the optical nonlinear dimension for coding is theoretically boundless, yet practical considerations such as signal fluctuation must be taken into account. To avoid crosstalk, it is important to choose nonlinear applications that exhibit significant differences between samples. Looking ahead, the integration of the convolutional neural-network-based algorithm<sup>[7,38]</sup> for image recognition with PSF changes could pave the way for high-density multiplex imaging (Figures S16 and S17, Supporting Information). While our current demonstration involves two orthogonal color dimensions and 4 analytical channels, it is crucial to note that our proposed nonlinear dimension is fully orthogonal to existing coding dimensions. This enables seamless integration, resulting in a multiplied increase in available coding capability.

By leveraging the unique optical response of UCNPs, we successfully encode and decode their component information, simultaneously breaking the diffraction limit and enabling multiplexing in a single confocal image. We demonstrate the robustness of our method by accurately recognizing at least four species of UCNPs in a multiplexed imaging setup. It should be noted that, multiplexing of more particles with different doping information, e.g., composition, concentration, and maybe core-shell structure, could be realized if optimizing the signal-to-noise and optical setups. This work introduces a powerful dimension – optical nonlinearity – to the existing toolbox of multiplexed imaging of nanoparticles. The nonlinearity feature in multiplexing opens exciting possibilities for future research and development in nanoscale object recognition. Our work has the potential to be extended to various fields such as enhanced imaging and identification of nanoscale objects in complex biological systems and anti-counterfeiting, high-throughput analysis and detection of multiple targets simultaneously in microarray assays, deep tissue multiplexing detection in noninvasive diagnostics, and storing high-density data in a compact format.

## 4. Experimental Section

The experimental details are provided in the Supporting Information.

## Supporting Information

Supporting Information is available from the Wiley Online Library or from the author.

## Acknowledgements

L.D. and C.C. contributed equally to this work. The authors acknowledge the financial support from the National Natural Science Foundation of China Youth Science Foundation (Grant No. 12204102), the China Postdoctoral Science Foundation (Grant No. 2021M702581), the Australian Research Council Discovery Projects (Grant No. DP220101417), the

Australian Research Council Centre of Excellence for Transformative Meta-Optical Systems (Grant No. CE200100010), the Australian Research Council Future Fellowships (Grant No. FT220100053 to I.A.), the Australia National Health and Medical Council (Grant No. APP1177374 to Q.P.S.), and the Australia National Heart Foundation (Grant No. 102592 to Q.P.S.). [Correction added on 4 December 2023, after first online publication: CAUL funding statement has been added.]

Open access publishing facilitated by The Australian National University, as part of the Wiley - The Australian National University agreement via the Council of Australian University Librarians.

## Conflict of Interest

The authors declare no conflict of interest.

## Data Availability Statement

The data that support the findings of this study are available from the corresponding author upon reasonable request.

## Keywords

lanthanide, multiplexing, nonlinearity, super-resolution

Received: August 30, 2023

Revised: November 4, 2023

Published online:

- [1] C. J. Myers, M. Celebrano, M. Krishnan, *Nat. Nanotechnol.* **2015**, *10*, 886.
- [2] Y. Lu, J. Zhao, R. Zhang, Y. Liu, D. Liu, E. M. Goldys, X. Yang, P. Xi, A. Sunna, J. Lu, Y. Shi, R. C. Leif, Y. Huo, J. Shen, J. A. Piper, J. P. Robinson, D. Jin, *Nat. Photonics* **2014**, *8*, 32.
- [3] M. Xian, Y. Xu, X. Ouyang, Y. Cao, S. Lan, X. Li, *Sci. Bull.* **2020**, *65*, 2072.
- [4] X. Ouyang, Y. Xu, M. Xian, Z. Feng, L. Zhu, Y. Cao, S. Lan, B.-O. Guan, C.-W. Qiu, M. Gu, X. Li, *Nat. Photonics* **2021**, *15*, 901.
- [5] Y. Yang, Y. Chen, P. Pei, Y. Fan, S. Wang, H. Zhang, D. Zhao, B.-Z. Qian, F. Zhang, *Nat. Nanotechnol.* **2023**, *18*, 1195.
- [6] J. Luan, A. Seth, R. Gupta, Z. Wang, P. Rathi, S. Cao, H. Gholami Derami, R. Tang, B. Xu, S. Achilefu, J. J. Morrissey, S. Singamaneni, *Nat. Biomed. Eng.* **2020**, *4*, 518.
- [7] B. Liu, J. Liao, Y. Song, C. Chen, L. Ding, J. Lu, J. Zhou, F. Wang, *Nanoscale Adv.* **2022**, *4*, 30.
- [8] Z.-Y. Lyu, H. Dong, X.-F. Yang, L. Huang, Y.-J. Xu, K. Wu, L.-D. Sun, C.-H. Yan, *JACS Au* **2023**, *3*, 860.
- [9] Y. Sun, J. Wang, Q. Zeng, Y. Yang, C. Zhang, J. Li, H. Yu, *ChemRxiv* **2023**, 1.
- [10] R. Jungmann, M. S. Avendaño, J. B. Woehrstein, M. Dai, W. M. Shih, P. Yin, *Nat. Methods* **2014**, *11*, 313.
- [11] F. Wang, S. Wen, H. He, B. Wang, Z. Zhou, O. Shimoni, D. Jin, *Light: Sci. Appl.* **2018**, *7*, 18006.
- [12] H. H. Gorris, R. Ali, S. M. Saleh, O. S. Wolfbeis, *Adv. Mater.* **2011**, *23*, 1652.
- [13] M. Han, X. Gao, J. Z. Su, S. Nie, *Nat. Biotechnol.* **2001**, *19*, 631.
- [14] X. Li, T.-H. Lan, C.-H. Tien, M. Gu, *Nat. Commun.* **2012**, *3*, 998.
- [15] C. Chen, F. Wang, S. Wen, Q. P. Su, M. C. L. Wu, Y. Liu, B. Wang, D. Li, X. Shan, M. Kianinia, I. Aharonovich, M. Toth, S. P. Jackson, P. Xi, D. Jin, *Nat. Commun.* **2018**, *9*, 4.
- [16] B. Liu, C. Chen, X. Di, J. Liao, S. Wen, Q. P. Su, X. Shan, Z.-Q. Xu, L. A. Ju, C. Mi, F. Wang, D. Jin, *Nano Lett.* **2020**, *20*, 4775.



- [17] M. Lelek, M. T. Gyparaki, G. Beliu, F. Schueder, J. Griffié, S. Manley, R. Jungmann, M. Sauer, M. Lakadamyali, C. Zimmer, *Nat. Rev. Methods Primers* **2021**, 1, 39.
- [18] Y. Liu, Y. Lu, X. Yang, X. Zheng, S. Wen, F. Wang, X. Vidal, J. Zhao, D. Liu, Z. Zhou, C. Ma, J. Zhou, J. A. Piper, P. Xi, D. Jin, *Nature* **2017**, 543, 229.
- [19] K. Zhanghao, X. Chen, W. Liu, M. Li, Y. Liu, Y. Wang, S. Luo, X. Wang, C. Shan, H. Xie, J. Gao, X. Chen, D. Jin, X. Li, Y. Zhang, Q. Dai, P. Xi, *Nat. Commun.* **2019**, 10, 4694.
- [20] M. Bates, G. T. Dempsey, K. H. Chen, X. Zhuang, *ChemPhysChem* **2012**, 13, 99.
- [21] J. Bückers, D. Wildanger, G. Vicidomini, L. Kastrup, S. W. Hell, *Opt. Express* **2011**, 19, 3130.
- [22] T. Niehörster, A. Löschberger, I. Gregor, B. Krämer, H.-J. Rahn, M. Patting, F. Koberling, J. Enderlein, M. Sauer, *Nat. Methods* **2016**, 13, 257.
- [23] N. Oleksiiivets, Y. Sargsyan, J. C. Thiele, N. Mougios, S. Sograte-Idrissi, O. Nevskiy, I. Gregor, F. Opazo, S. Thoms, J. Enderlein, R. Tsukanov, *Commun. Biol.* **2022**, 5, 38.
- [24] X. Shan, F. Wang, D. Wang, S. Wen, C. Chen, X. Di, P. Nie, J. Liao, Y. Liu, L. Ding, P. J. Reece, D. Jin, *Nat. Nanotechnol.* **2021**, 16, 531.
- [25] L. Ding, X. Shan, D. Wang, B. Liu, Z. Du, X. Di, C. Chen, M. Maddahfar, L. Zhang, Y. Shi, P. Reece, B. Halkon, I. Aharonovich, X. Xu, F. Wang, *Adv. Sci.* **2022**, 9, 2203354.
- [26] N. Dubey, S. Chandra, *J. Rare Earths* **2022**, 40, 1343.
- [27] Y. Niu, Z. Bao, Y. Gao, M. Guo, J. Liu, J. Shao, M. Lu, Z. Yuan, X. Xie, *J. Rare Earths* **2023**.
- [28] C. Chen, L. Ding, B. Liu, Z. Du, Y. Liu, X. Di, X. Shan, C. Lin, M. Zhang, X. Xu, X. Zhong, J. Wang, L. Chang, B. Halkon, X. Chen, F. Cheng, F. Wang, *Nano Lett.* **2022**, 22, 7136.
- [29] C. Chen, B. Liu, Y. Liu, J. Liao, X. Shan, F. Wang, D. Jin, *Adv. Mater.* **2021**, 33, 2008847.
- [30] D. Denkova, M. Ploschner, M. Das, L. M. Parker, X. Zheng, Y. Lu, A. Orth, N. H. Packer, J. A. Piper, *Nat. Commun.* **2019**, 10, 3695.
- [31] S. De Camillis, P. Ren, Y. Cao, M. Plöschner, D. Denkova, X. Zheng, Y. Lu, J. A. Piper, *Nanoscale* **2020**, 12, 20347.
- [32] C. Lee, E. Z. Xu, Y. Liu, A. Teitelboim, K. Yao, A. Fernandez-Bravo, A. M. Kotulska, S. H. Nam, Y. D. Suh, A. Bednarkiewicz, B. E. Cohen, E. M. Chan, P. J. Schuck, *Nature* **2021**, 589, 230.
- [33] Y. Liang, Z. Zhu, S. Qiao, X. Guo, R. Pu, H. Tang, H. Liu, H. Dong, T. Peng, L.-D. Sun, J. Widengren, Q. Zhan, *Nat. Nanotechnol.* **2022**, 17, 524.
- [34] G. Zhao, M. M. Kabir, K. C. Toussaint, C. Kuang, C. Zheng, Z. Yu, X. Liu, *Optica* **2017**, 4, 633.
- [35] S. Wen, J. Zhou, K. Zheng, A. Bednarkiewicz, X. Liu, D. Jin, *Nat. Commun.* **2018**, 9, 2415.
- [36] Y. Liu, S. Wen, F. Wang, C. Zuo, C. Chen, J. Zhou, D. Jin, *Adv. Sci.* **2023**, 10, 2205990.
- [37] D. J. Gargas, E. M. Chan, A. D. Ostrowski, S. Aloni, M. V. P. Altoe, E. S. Barnard, B. Sani, J. J. Urban, D. J. Milliron, B. E. Cohen, P. J. Schuck, *Nat. Nanotechnol.* **2014**, 9, 300.
- [38] H. Ni, Z. Wu, X. Wu, J. G. Smith, M. J. Zachman, J.-M. Zuo, L. Ju, G. Zhang, M. Chi, *Nano Lett.* **2023**, 23, 7442.